Displacement Estimation With Co-Registered Ultrasound for Image Guided Neurosurgery: A Quantitative *In Vivo* Porcine Study

Karen E. Lunn*, Keith D. Paulsen, *Member, IEEE,* David W. Roberts, Francis E. Kennedy, Alex Hartov, *Member, IEEE,* and John D. West

***Abstract*—Brain shift during open cranial surgery presents a challenge for maintaining registration with image-guidance systems. Ultrasound (US) is a convenient intraoperative imaging modality that may be a useful tool in detecting tissue shift and updating preoperative images based on intraoperative measurements of brain deformation. We have quantitatively evaluated the ability of spatially tracked freehand US to detect displacement of implanted markers in a series of three *in vivo* porcine experiments, where both US and computed tomography (CT) image acquisitions were obtained before and after deforming the brain. Marker displacements ranged from 0.5 to 8.5 mm. Comparisons between CT and US measurements showed a mean target localization error of 1.5 mm, and a mean vector error for displacement of 1.1 mm. Mean error in the magnitude of displacement was 0.6 mm. For one of the animals studied, the US data was used in conjunction with a biomechanical model to nonrigidly re-register a baseline CT to the deformed brain. The mean error between the actual and deformed CT's was found to be on average 1.2 and 1.9 mm at the marker locations depending on the extent of the deformation induced. These findings indicate the potential accuracy in coregistered freehand US displacement tracking in brain tissue and suggest that the resulting information can be used to drive a modeling re-registration strategy to comparable levels of agreement.**

***Index Terms*—Brain modeling, brain shift, image-guided neurosurgery, image registration, intraoperative ultrasound.**

I. Introduction

ONE of the important challenges facing image-guided neurosurgery is the fact that in open cranial procedures, the brain deforms significantly over the course of an operation, resulting in a loss of registration with its corresponding preoperative images [1]–[5]. Consequently, the navigational utility of the image guidance system is diminished. Given the desire for a high-resolution, high-contrast image volume which accurately depicts the current surgical scene, this loss of registration could be corrected by either acquiring a new high-quality scan [typically magnetic resonance (MR)], or by nonrigidly registering the original images to the deformed brain. The use of intraoperative MR (iMR) has shown considerable promise as a platform for image-guided neurosurgery [6]–[12], though it does face a number of barriers to widespread acceptance, including the high cost of operation (in addition to capitalization associated with purchase/siting), and the inefficiency involved in disrupting a procedure to acquire an MR image series in the operating room (OR). Cost based justification of an iMR unit may become difficult if less expensive, more convenient alternatives emerge.

Intraoperative ultrasound (US) potentially provides such an option. In recent work, Unsgaard *et al.* argue that the improved image quality of US over the past few years has made it an effective image-guidance tool, allowing successful localization of brain lesions in 112 out of 114 cases in their experience [13]. Many groups have extended the capability of two-dimensional (2-D) US by attaching three–dimensional (3-D) spatial tracking devices, and have demonstrated its utility in the OR for image guidance including its potential to track brain shift [14]–[21]. These spatially tracked US systems may be especially useful for their role in creating a "pseudo-MR"—a term coined by Bucholz *et al.* to describe an MR image that has been deformed to fit the data provided by the US image [15]. This approach appears to be an effective way to use US because the higher contrast resolution of the MR data is retained, yet the intraoperative US imaging provides real-time deformation data which can be used to update the MR image stack. Furthermore, matching the MR scan to the intraoperative US allows for more informed comparison of the two modalities.

Generating a pseudoscan that is adequate for surgical navigation requires accuracy in each of the following steps:

1) coregistering US with the preoperative scan.
2) detecting brain deformation using coregistered US.
3) deforming the preoperative image volume based on displacement data from US.

The process of obtaining a good initial coregistration is fairly well established, with several groups reporting the accuracy of their systems based on experiments involving static phantoms [20], [22]–[24]. Fewer studies have quantitatively investigated the second step—using coregistered US to capture the process of deformation. Exceptions include studies by Comeau *et al.* who used their US tracking system to measure displacement in their custom-built deformable gel phantom [16], and Pennec *et al.*, who tested their system's nonrigid performance by comparing measured and predicted volume changes of a balloon

Manuscript received July 11, 2003; revised August 24, 2003. This work was supported by National Institutes of Health (NIH) National Institute of Neurological Disorders and Stroke under Grant R01-NS33900. *Asterisk indicates corresponding author.*

*K. E. Lunn is with the Thayer School of Engineering, Dartmouth College, Hanover, NH 03755 USA (e-mail: Karen.E.Lunn@Dartmouth.edu).

K. P. Paulsen, F. E. Kennedy, A. Hartov, and J. D. West are with the Thayer School of Engineering, Dartmouth College, Hanover, NH 03755 USA.

D. W. Roberts is with the Dartmouth Hitchcock Medical Center, Lebanon, NH 03766 USA.

Digital Object Identifier 10.1109/TMI.2003.819293

catheter fixed in a postmortem pig brain [25]. Both groups also achieved the third step of nonrigidly registering the preoperative image. Comeau *et al.* relied on feature segmentation, calculating deformation by matching parametrically sampled splines of interior features from US and MR, then iteratively applying the deformation field to the entire 2-D plane of the coregistered MR image [16]. They report a target localization error (TLE) of 1.4 mm. Pennec *et al.* used an image-based approach: after rigidly registering MR images to US acquired before dura removal, they nonrigidly register subsequent US images to these baseline US sequences to determine the deformation field to apply to the MR [25]. Their system was determined to have an error of 0.4–0.17 cm^3 in measurements of balloon volume in a *post mortem* porcine brain.

A logical progression from these studies would be quantitative investigation of how well US can capture deformation in a challenging environment that captures more of the similarities of the operating room (OR), yet, still offers opportunities for accuracy assessment under controlled conditions that typically are not clinically possible. The OR creates the potential for registration degradation given the complexities of clinical cases, including the changing shape of the brain throughout surgery, the heterogeneity of brain tissue, pulsation due to cardiac and respiratory cycling, movement of the operating table, time constraints limiting the number of US images acquired, and the sparsity of US data that can be acquired with a spatially tracked freehand approach (rather than a fully 3-D scanhead). In addition to these potential sources of error, coregistration faces challenges at each stage of US to MR registration, including loss of accuracy in feature segmentation from US images, ambiguity in feature correspondence between image sets, error in tracking tools, imperfect patient registration (due to movement of fiducial markers, identification of markers in the MR, digitization of the markers with tracked stylus probes), and imperfect calibration of US trackers.

To quantify US coregistration and tracking accuracy in the presence of these factors, we have conducted a series of *in vivo* porcine brain experiments. For one of these cases, we incorporate the US data to deform the preoperative image volume, creating a pseudoscan using a model-based strategy. The results show that TLE of 1.5 mm on average can be maintained based on rigid registration and calibration procedures prior to deformation induction. Further, target displacement error (TDE) improves on average to 0.6 mm in magnitude (1.1 mm when also accounting for directional deviations) by comparing consecutive US scans to themselves, rather than repeatedly to the preoperative image volume when tissue deformation occurs. Similar errors (1–2 mm on average) occur in the localization of targets not tracked by US whose updated positions are determined from a model-generated pseudoimage volume enhanced by the US information.

It is important to recognize that scale of the porcine and human brains are considerably different and may modulate the study's findings. The smaller size of the porcine brain with respect to the human brain constrained the deformation to be within a centimeter of motion, which is less than that reported to occur clinically. However, as a percentage of volume, the relative deformation for these experiments was generally greater which has the net effect of accentuating the influence of boundary conditions on the internal deformation field relative to what might be expected in humans. Whether the uncertainty in boundary data amplifies errors between the measured and computed response in the smaller porcine brain or the more constrained magnitude of motion which occurs favorably biases these model estimates relative to human studies remains to be seen. While the issues of scale and the artificiality of the target tracking and surgical procedures used may limit the translation of these findings to human studies, they, nonetheless, bode well for prospects of US displacement tracking and lay a quantitative foundation for accuracy expectations in the OR against which future procedural and/or algorithmic improvements can be benchmarked.

II. Methods and Materials

A. Experimental Procedures

Motivated by both the desire to more closely simulate open-cranial surgery *in vivo* and the objective of obtaining reliable quantitative measurements of displacement from US, which could be validated unambiguously through concurrent volumetric imaging with an independent method, this study was designed as a series of three porcine experiments, where induced brain deformation was measured in both US and computed tomography (CT) images. We chose CT (over MR) because of its more rapid image-acquisition over the full brain volume once deformation was induced and compatibility with concurrent US imaging once the animal was positioned for volumetric scanning. We also elected to implant markers in the brain as gold standards (see below) in order to minimize errors associated with feature segmentation and identification across imaging methods which can act as confounding factors in accuracy studies relying on natural landmarks. The use of these markers minimized the penalty of loss of soft tissue contrast in CT relative to MR since the accuracy assessments did not rely on fine details of brain structure per se.

For all three animal subjects the procedure was the same and was approved by Dartmouth's Institutional Animal Care and Use Committee. After anesthetizing each subject and securing it in a custom-designed stereotactic frame, a craniotomy was performed. Next, 1-mm stainless-steel beads (which are clearly visible in both US and CT) were inserted into the pig's brain, in locations well distributed around the area of the cranial vault which would experience the most deformation. Gross morphological and histological analysis of implanted brains from prior studies [26] have shown that these markers cause minimal trauma and are well-adhered to the tissue, making them surrogate indicators of the surrounding tissue motion. Beads were also secured to the rim of the skull to use as fiducial markers for registration purposes. The pig was then transferred to the CT scanning room, where the remainder of the experiment took place.

First, a set of US and CT baseline images were acquired for the undeformed state of the brain. Next, the brain was deformed. For two of the experiments, deformation was induced by a small catheter balloon inserted along the cranial wall and inflated approximately to 1–2 cc. The third experiment used a plastic re-

tractor blade inserted along the midline of the brain to induce deformation. In all three cases, the brain was deformed and the source of deformation was fixed while another set of US and CT images were acquired. The pixel sizes of the CT scans ranged from 0.2 to 0.4 mm, and slice thickness was consistently 1.0 mm. For one of the balloon inflation experiments, a second level of deformation was induced by further expanding the balloon. In this case, a third set of images was acquired. The fiducial registration markers were digitized with the stylus probe to obtain the initial position of the animal and the new position any time that the animal was moved.

For each US set, over 85 images were acquired at a 6-cm depth scale setting. The images were recorded in freehand mode, and effort was made to capture multiple images of each implanted bead by sweeping back and forth across the region of interest (ROI), much as surgeons sweep across a target feature. This strategy was adopted to simulate the clinical setting where the surgeon may freely sweep back and forth over a target feature rather than being constrained to a predetermined pattern of acquisition. Certain beads were more difficult to visualize than others, and in those instances, fewer images were acquired. As such, the number of images per bead was variable, but ranged from a single image to more than ten images. For all three experiments, the time elapsed between each US and CT acquisition was approximately 5–10 min.

B. Extracting Bead Displacement Data

In order to compare displacement measurements from CT and US data, the beads from all US and CT scans must be extracted and then mapped to the baseline CT volume using a registration method. After initial registration, any differences between the beads from the two CT data sets (predeformation and postdeformation) or between those from the two US data sets were recorded as bead movement. Prior to measuring bead displacement, each marker had to be identified and its local coordinates recorded. The process of extracting beads from the CT and US scans is described in this section while the registration and calibration procedures for relating the two image spaces is presented in Section II-C.

As an initial step in processing CT data, the scans were imported into Analyze image software (Mayo Clinic Foundation, Rochester, MN). For each image stack, the coordinates of the beads implanted in the brain were manually recorded and saved for displacement calculations.

Determining the position of the beads in US was a more involved process. Our intraoperative US system consists of a SONOLINE Sienna Digital Ultrasound System (Siemens Medical Systems, Elmwood Park, NJ), with a 5-MHz curved array. For this study, the 6-cm depth scale was used. Due to the thickness of the US beam, inaccuracies in locating a point can result if it appears to be in the image, but is actually outside of the image plane. To reduce this source of error, we employed a semi-automatic technique for sensing the location of the beads in the US images. The method was designed to identify potential beads and discard them if the signal was either too weak or did not exhibit certain characteristics indicative of the US bead response when centered in the acquisition plane. Two matching criteria were used. First, the images were thresholded at 90% maximum intensity, and the centroids of the remaining connected components were calculated. Second, each centroid was tested to determine if it fit the characteristic US diffraction pattern for a bead. This was accomplished by calculating a profile of image intensity along the line emanating from the centroid and extending radially in the direction of the acoustic signal for a distance of approximately 50 pixels. The intensity profile was compared to the response of a "model" bead from a single US image that had been determined to represent the ideal in-plane bead profile selected from one of the best quality US images from out of all three experiments. The candidate point was accepted as a bead location only if the root mean square of the difference between its profile and the model distribution was less than 7% of the maximum intensity. Fig. 1 depicts the US image of the model bead and its profile plot to which intensity maps of all potential in-plane bead locations were compared. Note that this process

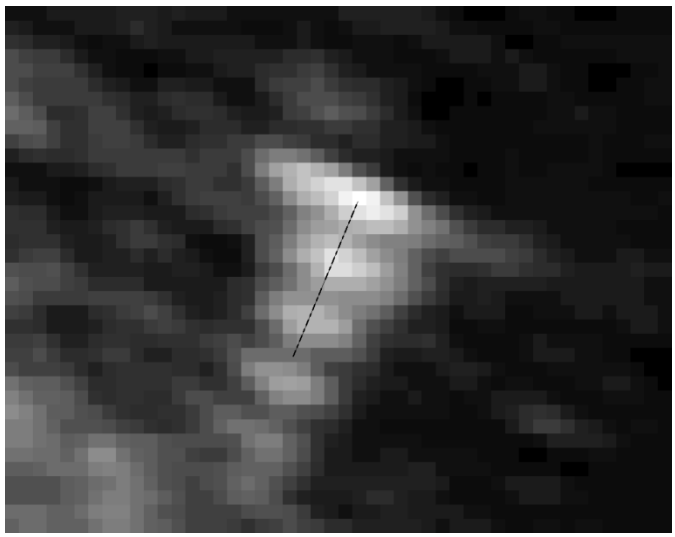

(a)

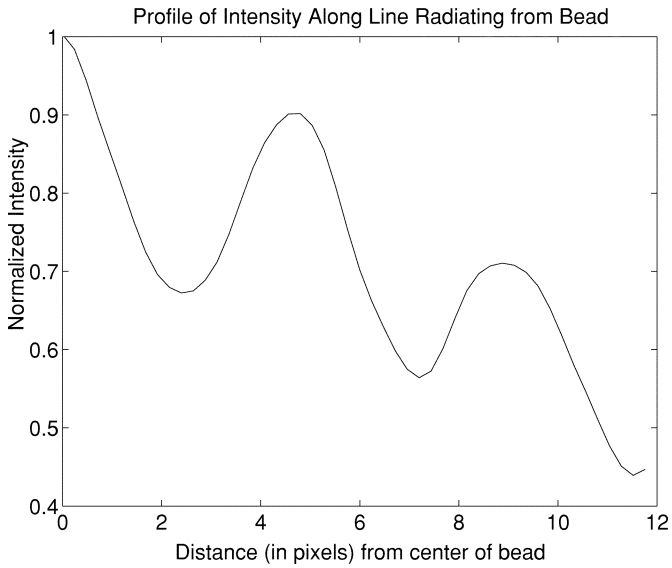

(b)

Fig. 1. Closeup of US image of model bead (a) and profile plot of intensity from the diffraction pattern of the model bead (b) that served as the testing pattern against which candidate bead positions were accepted (or rejected) as true in-plane bead locations.

of bead segmentation was based on three adjustable parameters: initial threshold (90%), distance from model and candidate bead over which the intensity profiles were compared (50 pixels), and matching criteria of the test profile to the model profile (less than 7% error). These parameters were chosen based on empirical evidence that they could adequately detect beads across all three studies.

The only manual step in this process was the option to discard a location that had been automatically chosen. This occurred in only few instances and in all cases the automatic technique had chosen a point which was obviously either skull or the second maximum of a diffraction pattern already selected. This semi-automatic extraction algorithm had the effect of screening out a portion of the beads that were difficult to image for various reasons. For example, in two instances, errors in bead placement resulted in two markers being nearly co-located. Because they were so close together, these beads were difficult to distinguish individually in the US image, and as a result were not detected by the bead extraction algorithm. This screening method also effectively filtered out beads that were too close to the scanhead to generate a sharp, clear signal. Images of beads that were less than a centimeter from the US transducer were blurred as a result of the thickness of the US image near the transducer. More than 90% of the beads extracted were located at a depth greater than one centimeter within the US image. Though only a few beads were within one centimeter of the brain surface, eliminating these locations from the calculations may have had the additional effect of reducing slight errors due to deformation induced by the pressure of US transducer applied to the exposed parenchyma during scanning. Nonetheless, the results of this study are valid for features located deeper than one centimeter from the scanhead, which is where US is most valuable since other tools such as an operating microscope could be used to track surface deformation.

C. Coregistered US System

Once the beads were detected, the points were mapped from US to CT coordinates through a process of coregistering each US image to the baseline CT scan. This registration process is achieved through the help of the Polaris optical tracking system (Northern Digital, Waterloo, Ontario, CAN), which includes a passive stylus probe, passive US tracker, and active US tracker. Passive tools have IR reflectors, while active tools utilize infra red emitting diodes that are visible to a 3-D tracking camera. Both types of US trackers were used in the experiments.

These tools provide sufficient information to register the US image to the preoperative image stack through a series of coordinate transformations such that for any point in US, the corresponding point in MR or CT can be determined by the

$$\mathbf{P}_{\mathrm{CT}} = {}^{\mathrm{CT}}\mathbf{T}_{w}\,{}^{w}\mathbf{T}_{\mathrm{tr}}\,{}^{\mathrm{tr}}\mathbf{T}_{\mathrm{US}}\mathbf{P}_{\mathrm{US}} \tag{1}$$

where $\mathbf{P}_{\mathrm{CT}}$ and $\mathbf{P}_{\mathrm{US}}$ are the points in CT (or MR) and US coordinates, scaled to mm, ${}^{\mathrm{tr}}\mathbf{T}_{\mathrm{US}}$ is the transformation from the US image plane to the US tracker, ${}^{w}\mathbf{T}_{\mathrm{tr}}$ is the transformation

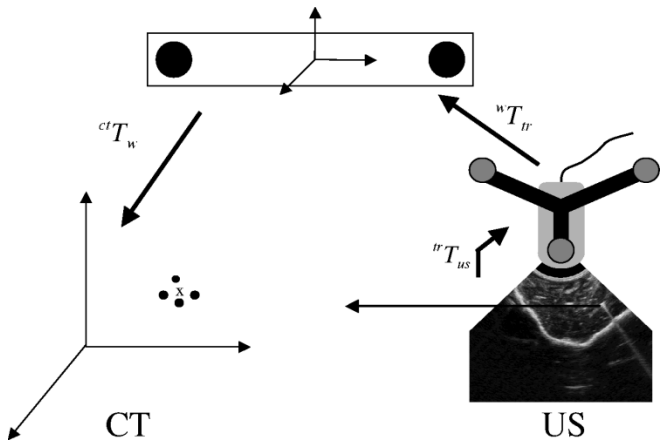

Fig. 2. Transformations required to map a point in US coordinates to CT. Starting from the US image, and moving counterclockwise the coordinate transformations are: from the US image plane to the US tracker $({}^{\mathrm{tr}}\mathbf{T}_{\mathrm{US}})$, from tracker to world coordinates $({}^{w}\mathbf{T}_{\mathrm{tr}})$, and from world to CT coordinates $({}^{\mathrm{CT}}\mathbf{T}_{w})$.

from tracker to world coordinates, and ${}^{\mathrm{CT}}\mathbf{T}_{w}$ is the transformation from world to CT coordinates, as illustrated in Fig. 2. The $\mathbf{P}$ matrices are of the form

$$\mathbf{P} = \begin{bmatrix} x_1 & x_2 & \dots & x_n \\ y_1 & y_2 & \dots & y_n \\ z_1 & z_2 & \dots & z_n \\ 1 & 1 & \dots & 1 \end{bmatrix} \tag{2}$$

for n number of points while the $\mathbf{T}$ matrices are written as

$$\mathbf{T} = \begin{bmatrix} & & & \\ & \mathbf{R}_{3\times 3} & & \begin{pmatrix} \Delta x \\ \Delta y \\ \Delta z \end{pmatrix} \\ & & & \\ 0 & 0 & 0 & 1 \end{bmatrix} \tag{3}$$

where (3) contains both the rotation $(\mathbf{R}_{3\times 3})$ and translation $(\Delta x, \Delta y, \Delta z)$ components of the transformation necessary to map points in US $(\mathbf{P}_{\mathrm{US}})$ to points in CT $(\mathbf{P}_{\mathrm{CT}})$.

The transformation from world to CT coordinates $\left({}^{\mathrm{CT}}\mathbf{T}_{w}\right)$, is determined by a point-based registration, where the locations of fiducial markers in world coordinates, $\mathbf{P}_{w}$, and in CT coordinates (scaled to mm), $\mathbf{P}_{\mathrm{CT}}$, are determined and the two sets of points are related through the overdetermined matrix equation

$$\mathbf{P}_{\mathrm{CT}} = {}^{\mathrm{CT}}\mathbf{T}_{w}\mathbf{P}_{w}. \tag{4}$$

This equation can easily be solved for ${}^{\mathrm{CT}}\mathbf{T}_{w}$ through a least squares fit using singular value decomposition (SVD) to preserve the orthogonality and scaling of the transformation matrix. The passive stylus probe that is used to digitize fiducial markers has been previously found to have a mean error of 0.3 to 0.6 mm for different tests of point reconstruction [27]. Registration error specific to this study is reported in the Section III.

The second transformation matrix, ${}^{w}\mathbf{T}_{\mathrm{tr}}$, is given by the Polaris software, and is dependent on the accuracy of each tracking tool. Northern Digital reports an accuracy of 0.35 mm for each marker on a tool [28].

The transformation matrix ${}^{\mathrm{tr}}\mathbf{T}_{\mathrm{US}}$ is obtained through a calibration procedure, similar to that used by Comeau *et al.* [16]. The calibration phantom consists of N-shaped wires suspended

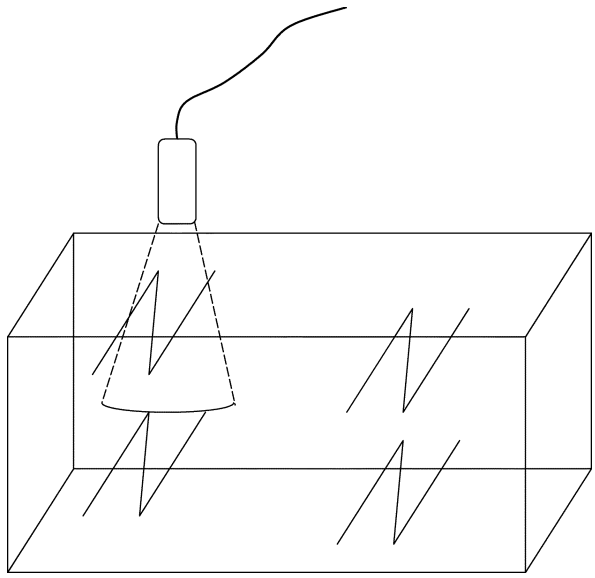

(a)

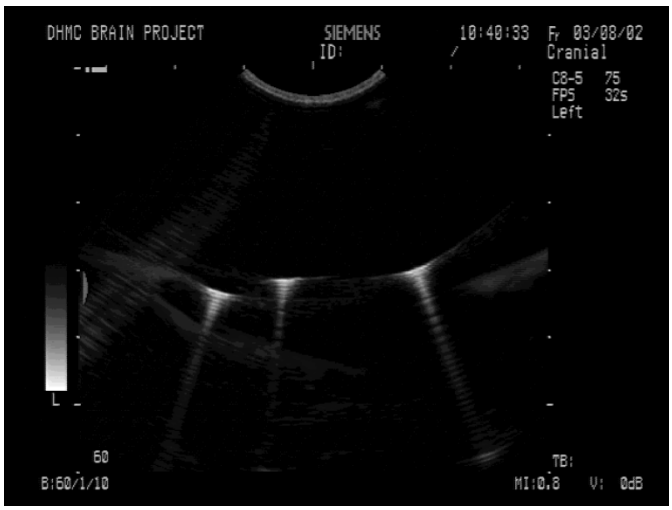

(b)

Fig. 3. Schematic of calibration tank (a) and US image of N-wires in tank (b).

in a water bath, as depicted in Fig. 3(a). US and CT images of the wires are acquired and by measuring the relative geometry of the cross section of the wires in the US images, the corresponding location of those points could be determined in world coordinates, and ultimately in CT coordinates (using ${}^{\mathrm{CT}}\mathbf{T}_w$). As with the patient to CT registration, by matching these points with a least squares fit and singular value decomposition, the rotation and translation components can be determined. After obtaining the calibration transformation matrix, the US coordinates of the wires were mapped into CT coordinates, and the distance between those mapped points and the actual CT coordinates were compared. The mean error was found to be between 1.4 and 2.1 mm for the three cases.

After extracting the beads, as described in Section II-B, the points were mapped from US to CT (1). Since there were several US images of each bead, this process resulted in a cluster of points for each marker, presumably due to a combination of factors including probe tracking error, US/tracker calibration error, and US image thickness. For each point cloud, the maximum distance from one point to another was less than 4 mm. The centroids of these clusters were found and recorded as the US-based location of the beads. Since all of the beads were not always visible, only those that could be detected in images for both the deformed and undeformed states of the brain were tracked and reported in Section III. Approximately half of the total number of implanted beads were available for analysis based on this process.

III. Results

A. Static Registration Accuracy

Two measures of registration accuracy were employed. The fiducial registration error (FRE) is defined as the root mean square error in the location of registration points in CT coordinates, and in world coordinates, mapped to CT, or

$$\mathrm{FRE}^2 \equiv \frac{1}{N}\sum_{i=1}^{n}(\mathbf{P}_{\mathrm{CT}_i} - {}^{\mathrm{CT}}\mathbf{T}_w\mathbf{P}_{w_i})^2. \tag{5}$$

For each case, the pig was initially registered to the baseline CT, and then registered again after the brain had been deformed (to account for motion of the subject between CT scans). This resulted in the computation of five registrations: two each for the subjects whose brains were deformed once, and three for the subject that underwent two stages of deformation. The FRE for these registrations ranged from 0.2 mm to 0.7 mm.

Perhaps a more useful measure of accuracy in static points is TLE, which computes error at the ROI or "target." After extracting the location of implanted beads from US and CT images and registering them to the baseline CT coordinates, TLE was calculated as the absolute difference between the CT points $(\mathbf{P}_{\mathrm{CT}})$ and the US points mapped to CT $(\hat{\mathbf{P}}_{\mathrm{CT}})$. This was done for each of the three cartesian coordinates. For example, error in the x direction is defined as

$$\mathbf{E}_x = |\mathbf{P}_{\mathrm{CT},x} - \hat{\mathbf{P}}_{\mathrm{CT},x}|. \tag{6}$$

TLE was also calculated as a vector error $(\mathbf{E}_r)$, which is simply the distance between the beads after registration, defined by

$$\mathbf{E}_r = \| \vec{\mathbf{E}} \| . \tag{7}$$

Using these definitions to compare initial and final (and also intermediate for one case) positions of the beads, the mean vector error for all stages of all three subjects was 1.5 mm. The mean, maximum, and standard deviations for the cartesian and vector errors are reported in Table I.

Fig. 4 depicts an US image and its corresponding oblique CT reconstruction. The crosshairs in both images are set to the coordinates found using the semi-automatic bead extraction algorithm described in Section II-B.

One might expect to observe a lever-arm effect resulting in greater error for beads that are further from the fidicial registration markers. However, the scatterplot shown in Fig. 5 indicates otherwise. With a correlation coefficient of -0.2, it appears that a bead's distance from the fiducial markers did not significantly

TABLE I
TARGET LOCALIZATION ERROR (TLE): DIFFERENCE BETWEEN TRUE CT COORDINATES AND US COORDINATES MAPPED TO CT SPACE OF IMPLANTED BEAD MARKERS. MEAN, MINIMUM (MIN), MAXIMUM (MAX), AND STANDARD DEVIATION (STD) FOR ALL THREE EXPERIMENTS COMBINED, IN THE x, y, AND z DIRECTIONS, AND AS A VECTOR SUM

	E_x (mm)	E_y (mm)	E_z (mm)	E_r (mm)
mean	1.0	0.7	0.6	1.5
min	0.1	0.1	0.0	0.5
max	2.2	2.9	1.8	3.1
std	0.6	0.5	0.4	0.6

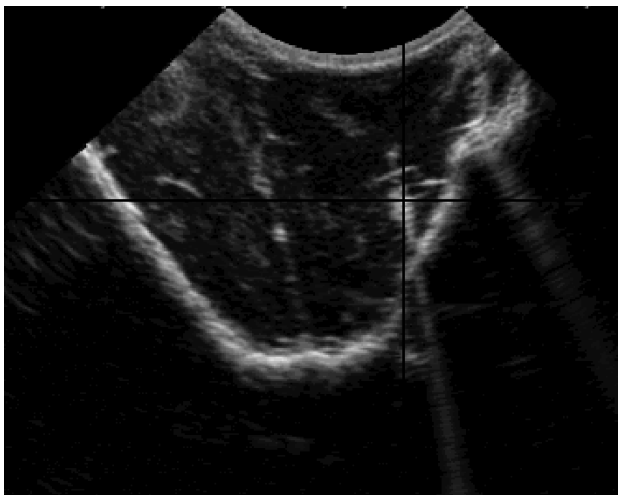

(a)

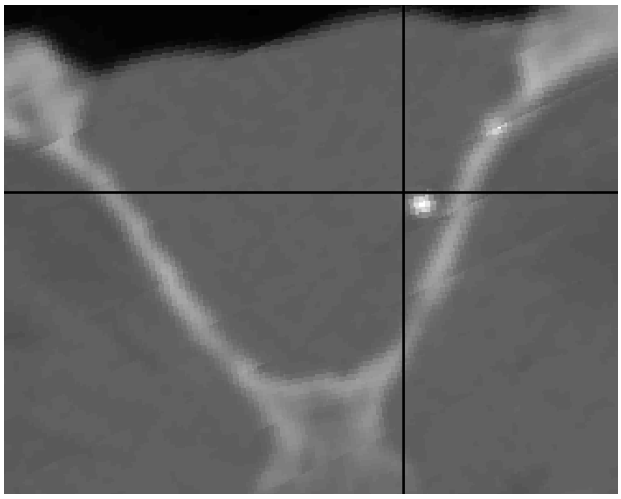

(b)

Fig. 4. US image of bead (a) and corresponding CT reconstruction (b). Crosshairs are set on a bead in US image and overlaid at the transformed coordinate position in the CT image volume.

affect the error in US bead localization. This finding suggests that other sources of error play a more dominant role.

B. Displacement Accuracy

Having registered the beads to baseline CT coordinates, the displacement of each bead can easily be calculated. For each marker, we have two measurements of displacement—from the

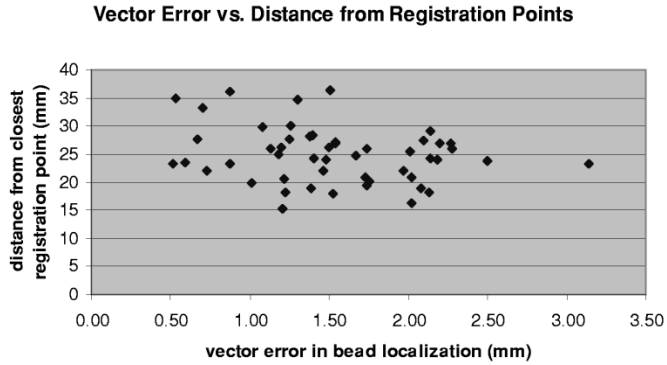

Fig. 5. For each bead identified by US, the vector sum of TLE is plotted against its distance from the closest fiducial registration marker.

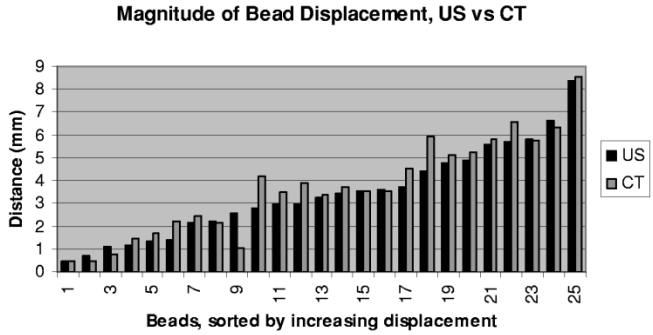

Fig. 6. Bar graph showing the magnitude in displacements for US and CT. Beads are sorted by increasing displacement in US.

US data and from the CT data. The bar graph in Fig. 6 shows the US and CT value of the magnitude of displacements for all of the beads tracked. As evident from the graph, distances traveled by the beads ranged from under 1 mm to over 8 mm, and in most cases the US and CT measurements matched to less than 1 mm.

The TDE is determined by comparing displacements measured from CT with corresponding values from US. It is reported as the difference between cartesian components of displacement (for example, error in x is $\mathbf{E_{\Delta x}}$), and as the vector sum of errors, where an individual vector error ($\mathbf{E_v}$) is defined by

$$\mathbf{E_v} = \sqrt{\mathbf{E}^2_{\mathbf{\Delta x}} + \mathbf{E_{\Delta}y}^2 + \mathbf{E_{\Delta}z}^2}. \tag{8}$$

Finally, the magnitudes of displacement are computed in each modality, and the difference between those values for CT and US is reported in Table II, which includes mean, maximum and standard deviations of cartesian, vector, and magnitude errors. Vector error in displacement calculations averaged 1.1 mm, and mean error in magnitude of displacement (distance) is even less at 0.6 mm.

Qualitatively, the match between US-based measurements of bead displacement and CT-based measurements is illustrated in Fig. 7. In this graphic, trajectories of bead motion for one of the cases is plotted for both US (stars) and CT (circles) within a wireframe mesh representing the deformed porcine brain. The indentation on the left side of the mesh indicates the position of the inflated balloon, and bead motion is approximately from left to right.

TABLE II
TDE: ERROR IN BEAD DISPLACEMENTS MEASURED IN US AS COMPARED WITH CT FOR ALL THREE EXPERIMENTS. MEAN, MINIMUM (MIN), MAXIMUM (MAX), AND STANDARD DEVIATION (STD) FOR x, y, AND z COMPONENTS OF ERROR, VECTOR ERROR, AND ERROR IN MAGNITUDE OF DISPLACEMENT (D)

	$E_{\Delta \mathbf{x}}$ (mm)	$E_{\Delta \mathbf{y}}$ (mm)	$E_{\Delta \mathbf{z}}$(mm)	$E_{\mathbf{v}}$ (mm)	E_d (mm)
mean	0.5	0.6	0.6	1.1	0.6
min	0.0	0.1	0.0	0.3	0.0
max	1.5	2.6	2.9	3.9	1.7
std	0.4	0.5	0.6	0.7	0.4

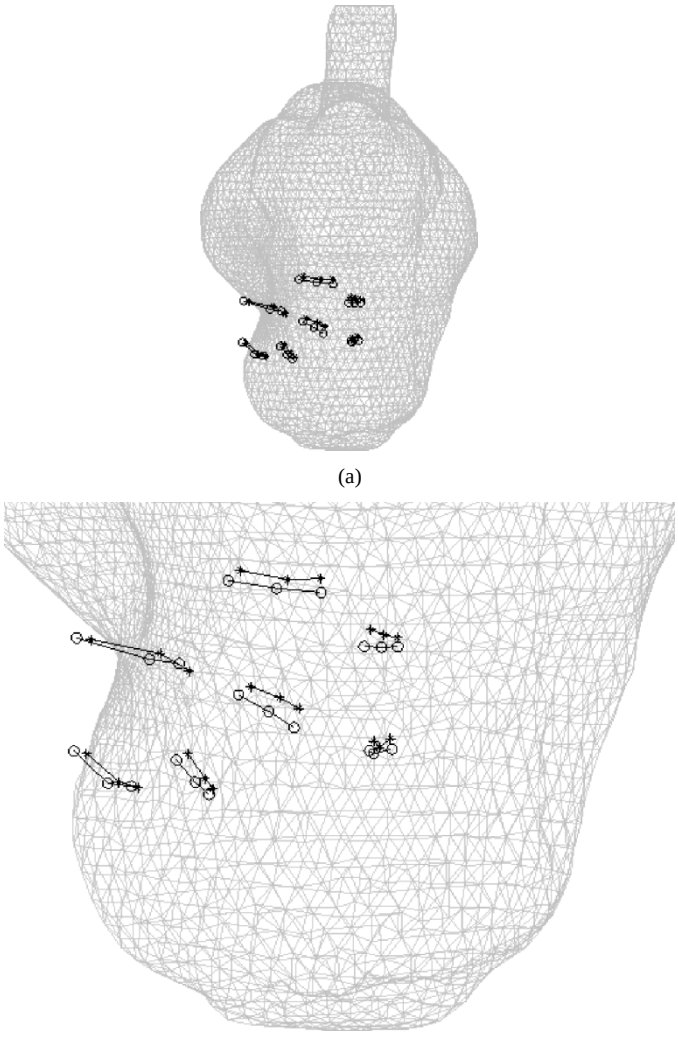

(a)

(b)

Fig. 7. (a) Trajectory of beads for the third pig experiment, shown overlaid on a volumetric mesh of the brain after balloon inflation and (b) closeup of region of interest. Note the indentation of the mesh on the left side of the figure, indicating the location of the inflated balloon.

IV. MODEL-BASED DEFORMING OF PREOPERATIVE SCAN

Recognizing that US alone may be insufficient for navigational purposes, the displacement data from US can be used to deform a preoperative high-resolution scan. However, US data is often limited because the images can be difficult to interpret and the range of image acquisition may represent only a subregion of the brain. As a result, interpolation and extrapolation of the displacement data can be challenging. The use of a biomechanical model may be well suited for this task, since the full deformation map is constrained by physical laws. In our experience, the boundary and driving conditions play a dominant role in determining the deformation field computed by such models. As an illustration of incorporating partial volume displacement information obtained from coregistered US tracking to generate constrained full-volume pseudoimage updates which account for surgically induced tissue deformation, we estimated critical model parameters from the US data and nonrigidly registered the baseline CT to the deformed brain for the third subject. The intraoperative CT acquired at the time of the deformation was used as the gold standard for assessing the quality of the US guided model update.

In the present experiments, the primary challenge in assigning boundary conditions is determining the location of the balloon catheter and the magnitude of tissue deformation on the balloon front. To limit the number of variables in a parameter search, the displacement at the balloon surface was *a priori* constrained to the shape of a Gaussian curve, whose standard deviation and maximum value were determined by the search process. The craniotomy location and boundaries for the search region were based on digitization of the fiducial registration markers attached to the rim of the craniotomy that were visible in the preoperative scans. Fig. 8 indicates the locations tested as candidates for the center of the balloon catheter. Also shown are the regions specified with our standard brainstem and craniotomy boundary conditions. Appendix A describes the optimization procedure used to find the balloon related parameters (location, shape, and magnitude). In short, the algorithm exhaustively tested 30 possible balloon catheter locations, followed by five different shapes of the Gaussian curve. At each iteration, US measurements for the displacement of feature locations (beads) were compared to the model calculations for those same positions. The boundary conditions that gave the best fit between the US data and model were characterized by a Gaussian curve with a standard deviation of 0.75 cm and a magnitude of 1.1 cm at the balloon origin (which was found to be located at the circled star in Fig. 8).

After identifying the appropriate boundary conditions from the US feature data, the preoperative CT was deformed according to the displacement field generated by this model run. The results of the warping algorithm are presented in Fig. 9, which shows actual images and model-based updates for three slices of the CT scan. The error in the procedure was quantified by comparing the new location of beads in the pseudo-CT image to their location in the actual (intraoperative) CT for each deformation using the remaining beads that were not part of the US data which guided the model update.

V. DISCUSSION AND CONCLUSION

It is interesting to compare the TLE results found in this study with other groups. Pagoulatos *et al.*, who use a magnetic tracking device, report a mean TLE of between 2.0 and 3.6 mm, varying with depth of the target [20]. Several groups have reported increased accuracy using optical tracking devices—Lindseth *et al.*, Comeau *et al.*, and Blackall *et al.* report TLE measurements of 1.40, 1.3, and 1.2 mm for their respective

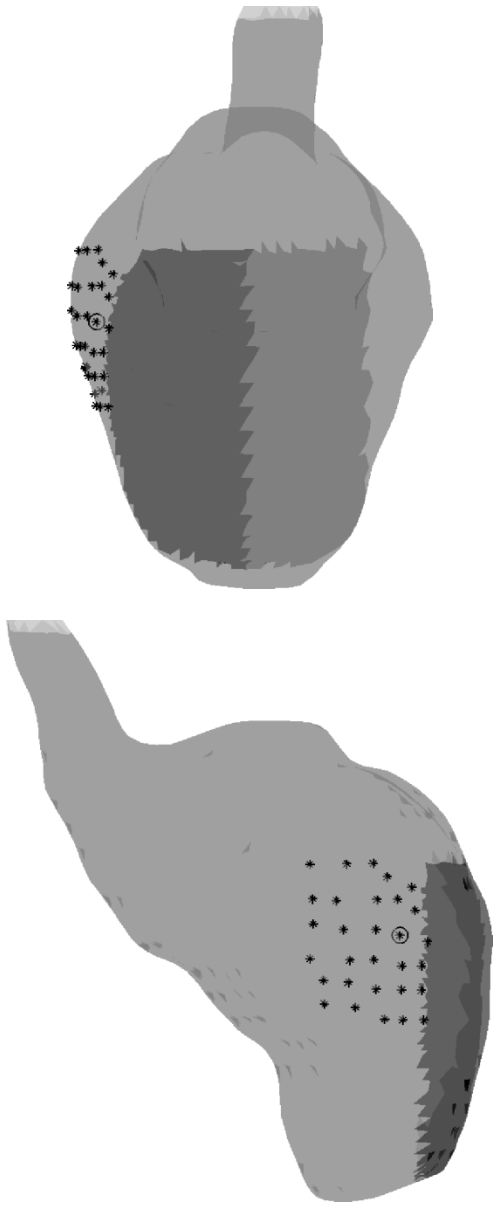

Fig. 8. Mesh for brain deformation model, shown in two orientations. The shaded rectangular areas on the superior portion of the brain represent the craniotomy region. On the left, darker side the dura was intact, while on the right, lighter side the dura was removed. The black stars show the 30 points that were tested as possible balloon catheter locations, and the circled position was the site determined by incorporating US data. Other boundary conditions included free fluid flow and stress free at the brainstem; free fluid flow and stress free on the left side of the craniotomy (dura removed); no fluid flow and stress free on the right side of the craniotomy (dura intact); no flow, stress free in tangential direction, and normal displacement at cranium wall decreasing as a function of distance from the balloon catheter (with maximum displacement at the balloon center and zero normal displacement far from balloon center defined by the Gaussian shape of the balloon front determined from US).

US tracking systems [16], [23], [24]. Pennec *et al.* did not measure TLE, but do document an error of 0.4 to 0.17 cm^3 in their measurement of the volume of a balloon using coregistered US [25]. In an earlier study, Barry *et al.* similarly compare volume measurements, finding an accuracy of less than 0.1 mL in reconstruction of a water-filled balloon [22]. We found that in live porcine brain, our system could achieve a mean TLE of 1.5 mm, indicating that our registration errors are comparable to those reported by other groups.

Quantitative displacement error calculations are not readily available in the literature. At a mean error of 0.6 mm (or 1.1 mm including directional error), the US-based displacement calculations reported here show significant improvement over TLEs found by our group as well as others. This low error leads to two important observations. First, US has the potential to be a suitably accurate method for tracking brain shift. With precise registration we can track points to an accuracy of less than a millimeter, which is less than the resolution of a standard MR scan of the brain. Despite this success, we recognize that the possibility of having point-like brain features to track in clinical cases is unrealistic, and that the additional challenge of fitting surfaces, rather than points, may increase error in the system due to the difficulty in extracting surfaces from US images. On the other hand, the additional information contributed by data from surfaces of interior structures would further constrain the model estimates, and could instead improve overall match between the updated preoperative image scan and the deformed brain. The use of nonrigid image-based registration schemes such as proposed by Pennec is likely to be an effective means of extracting displacement data from surfaces in US images [25]. While perhaps limited by the utilization of points instead of surfaces, the study described here has the value of demonstrating the accuracy that can potentially be achieved by coregistered US images and serves as a benchmark for comparing future efforts targeted at surface tracking. Furthermore, it is reasonable to assume that unless point-based measurements of displacement can be achieved accurately, the results of surface-based methodologies will be unreliable; therefore, ensuring point-based accuracy is an important initial step. Second, the greater accuracy in tracking displacement over absolute point localization indicates that care should be exercised in the way in which displacement data from US is used. The results presented here suggest that better accuracy in measuring brain shift can be achieved by comparing subsequent US sequences, rather than by comparing each US sequence to the preoperative scan. That is, if a bias is present in the coregistration process (due to error in the US to tracker calibration or inaccurate patient registration, for example), then some of this error may be absorbed by calculating displacement based on two sets of US images. This simple concept is illustrated in Fig. 10, where the MR and US measurements of two points do not coincide, and a better estimate of displacement is achieved by subtracting US coordinates.

With this observation in mind, displacement data from US-to-US comparisons were used to guide a biomechanical model that updated the preoperative CT. The use of a physically based model may be able to generate a reasonable deformation field for regions of the brain that are either not covered by the US images, or for which no features are easily extracted from the US field of view. This hypothesis is supported by our findings, reported in Table III, of an average 1.9-mm vector error for the displacement of all 18 markers, when US data from only five markers was used to guide the model estimates. In this way, the model is used to extrapolate and interpolate a full deformation field from the sparse US data.

Several studies have indicated the importance of using multiple sequences of intraoperative images frequently acquired throughout a case given the complexity of brain deformation

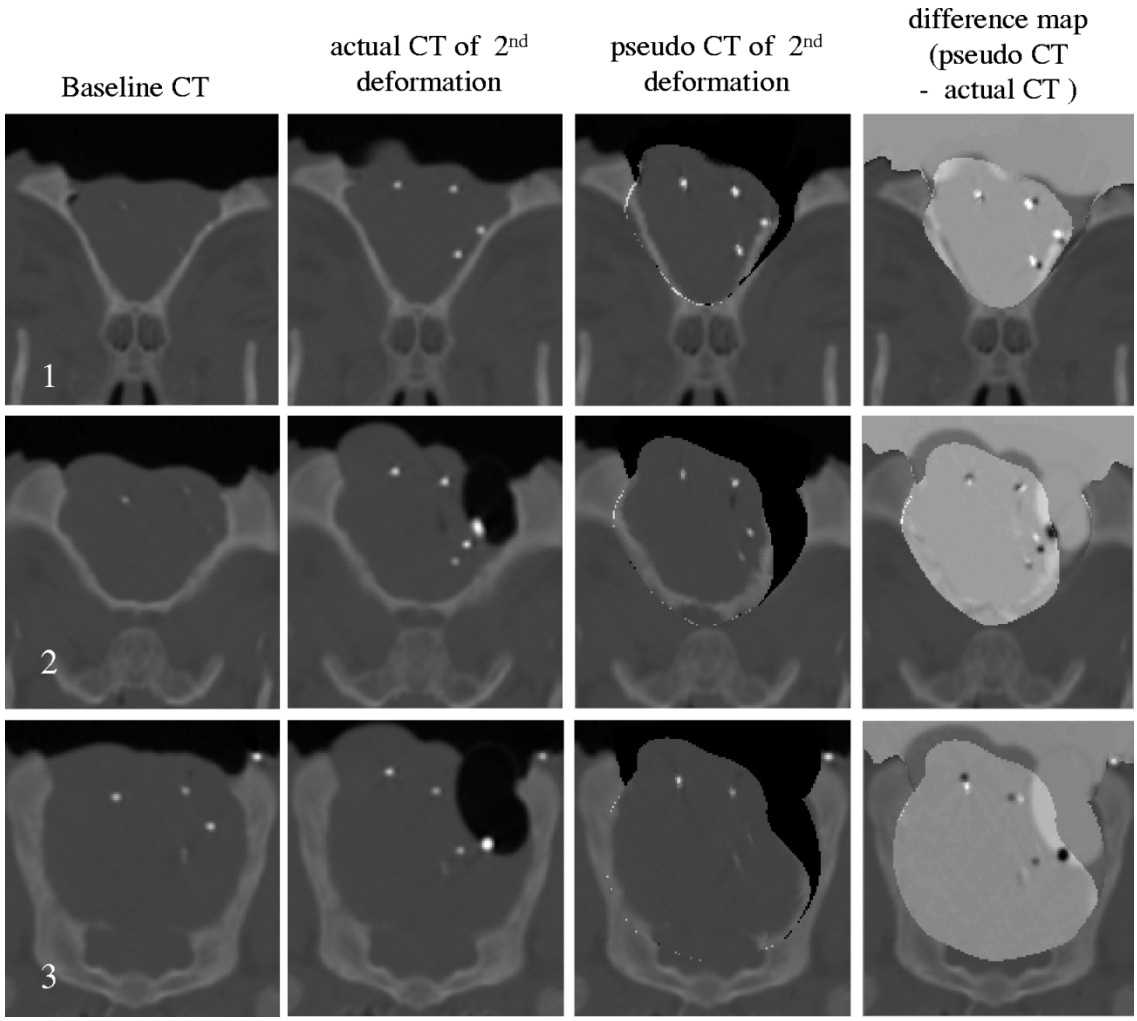

Fig. 9. Three transverse slices from the CT of the second deformation of the third pig, ranging from a slice rostral to the balloon (row 1), to a slice through its mid-region (row three). From left to right, the columns show slices from the original CT prior to deformation; the CT image after the second inflation of the balloon; the deformed (or pseudo) CT of the second inflation based on US data combined with the biomechanical model; and the difference in the parenchyma between the actual CT after the second deformation and and the model-based pseudo-CT, where the actual CT appears darker (e.g., the implanted fiducial markers appear black) than the pseudo-CT (where the markers appear are white).

TABLE III
DIFFERENCES BETWEEN MEASURED BEAD LOCATION IN ACTUAL CT AND IN MODEL-BASED PSEUDO-CT FOR FIRST AND SECOND DEFORMATIONS OF THIRD PIG. MEAN, MINIMUM (MIN), MAXIMUM (MAX), AND STANDARD DEVIATION (STD) FOR x, y, AND z COMPONENTS OF ERROR, VECTOR ERROR, AND ERROR IN MAGNITUDE OF DISPLACEMENT (D)

		$E_{\Delta \mathbf{x}}$ (mm)	$E_{\Delta \mathbf{y}}$ (mm)	$E_{\Delta \mathbf{z}}$(mm)	$E_{\mathbf{v}}$ (mm)	E_d (mm)
first	mean	0.7	0.7	0.5	1.2	0.7
deformation	min	0.1	0.0	0.0	0.5	0.1
	max	1.6	1.6	1.3	2.1	1.9
	std	0.4	0.4	0.4	0.4	0.5
second	mean	1.0	1.1	0.7	1.9	1.2
deformation	min	0.2	0.1	0.0	0.9	0.0
	max	2.8	2.9	1.7	3.6	3.4
	std	0.8	0.8	0.5	0.8	0.9

and its dynamic characteristics [2], [29]–[31]. The results of this porcine study indicate that coregistered US has the potential to be an effective and accurate means of measuring displacement, even in the complex environment of a deformable, *in vivo* brain, and that when combined with a computational model, may provide additional navigational power. However, it remains to be seen whether this method can ultimately estimate brain shift in more complicated clinical cases given the dynamic variations of deformation observed in recent studies [2], [29]–[31]. Furthermore, future research is needed to meet the challenge of

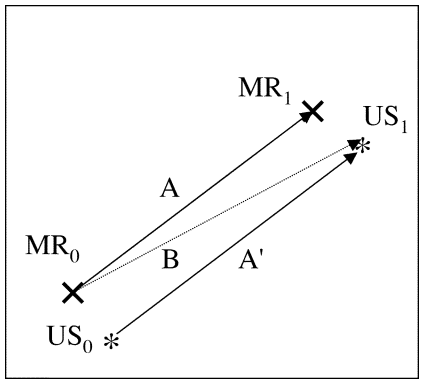

Fig. 10. Representation of measured displacements from US and MR. A better match to path A could be achieved by comparing US1 to the earlier US data (path A′) than from comparing US to the MR (path B).

extracting displacement data from the surfaces of interior brain structures (rather than the artificially introduced point markers used here).

APPENDIX
ULTRASOUND-GUIDED BOUNDARY CONDITION SEARCH

The search for the balloon's center and the shape of the Gaussian curve defining its deforming front consisted of thhe following three steps.

1) **Define the region of possible placements**. The region of possible balloon placements was estimated based on observations from the experimental setup. The catheter was known to be inserted on the right, rostral side of the craniotomy, approximately 1 to 2 cm deep and along the cranium wall. These specifications served to define a 2.5 $\times$2.0 cm search region. While the balloon placement could have been easily estimated from the intraoperative CT scans, the CT data was purposefully not used in order to simulate OR conditions where a high-resolution, full-volume intraoperative image scan would not be available.
2) **Search for best position within the region defined in Step 1.** To limit the optimization search, the algorithm did not test every combination of possible boundary conditions. Instead, it first tested the balloon location, which was assumed to exert a greater influence on the deformation, and then used the determined balloon coordinates to find the best standard deviation of the predefined Gaussian surface. For each of 30 different balloon positions within the placement region identified in step 1, the following calculations were made.
    a) Compute the model displacement field using a Gaussian distribution, with standard deviation of 1.0 cm and a maximum value of 0.5 cm at the balloon coordinates.
    b) Sample these solutions at the five locations corresponding to the feature (bead) coordinates as measured from US data.
    c) Weight the displacement solution by the constant value that produces the least-squares best fit between the US measurements and the model calculation at those five locations. Since the model equations are linear, weighting the boundary conditions by a constant scaling increases (or decreases) the interior displacements by the same factor. Therefore, we find the appropriate magnitude of the Gaussian curve by weighting the model solution to generate a best (least-squares) fit at the data points.

    The balloon location that minimized overall model-data misfit (at the five selected locations in US) was chosen to be the best set of boundary conditions.
3) **Search for the best distribution width at the optimal balloon center.** Based on the optimal balloon center found in step 2, an exhaustive search over five possible standard deviations for the Gaussian displacement profile describing the expanding balloon front was performed using the same least-squares model-data misfit criterion at the five feature locations derived from US.

ACKNOWLEDGMENT

The AnalyzeAVW software was provided in collaboration with the Mayo Foundation.

REFERENCES

[1] N. L. Dorward, O. Alberti, B. Velani, F. A. Gerritsen, W. F. Harkness, N. D. Kitchen, and D. G. Thomas, "Postimaging brain distortion: Magnitude, correlates, and impact on neuronavigation," *J. Neurosurg.*, vol. 88, pp. 656–662, 1998.
[2] T. Hartkens, D. L. G. Hill, A. D. Castellano-Smith, D. J. Hawkes Jr, C. R. Maurer, A. J. Martin, W. A. Hall, H. Liu, and C. L. Truwit, "Measurement and analysis of brain deformation during neurosurgery," *IEEE Trans. Med. Imag.*, vol. 22, no. 1, pp. 82–92, Jan. 2003.
[3] D. L. Hill Jr, C. R. Maurer, R. J. Maciunas, J. A. Barwise, J. M. Fitzpatrick, and M. Y. Wang, "Measurement of intraoperative brain surface deformation under a craniotomy," *Neurosurgery*, vol. 43, pp. 514–528, 1998.
[4] C. R. Maurer, D. L. G. Hill, A. J. Martin, H. Liu, M. McCue, D. Rueckert, D. Lloret, W. A. Hall, R. E. Maxwell, D. J. Hawkes, and C. L. Truwit, "Investigation of intraoperative brain deformation using a 1.5-T interventional MR system: Preliminary results," *IEEE Trans. Med. Imag.*, vol. 17, pp. 817–825, Oct. 1998.
[5] D. W. Roberts, A. Hartov, F. E. Kennedy, M. I. Miga, and K. D. Paulsen, "Intraoperative brain shift and deformation: A quantitative analysis of cortical displacement in 28 cases," *Neurosurgery*, vol. 43, no. 4, pp. 749–760, Oct. 1998.
[6] P. M. Black III, E. Alexander, C. Martin, T. Moriarty, A. Nabavi, T. Z. Wong, R. B. Schwartz, and F. Jolesz, "Craniotomy for tumor treatment in an intraoperative magnetic resonance imaging unit," *Neurosurgery*, vol. 45, pp. 423–433, 1999.
[7] M. Ferrant, A. Nabavi, B. Macq, P. M. Black, F. A. Jolesz, R. Kikinis, and S. K. Warfield, "Serial registration of intraoperalive MR images of the brain," *Med. Image Anal.*, vol. 6, pp. 337–359, 2002.
[8] M. Hadani, R. Spiegelmen, Z. Feldman, H. Berkenstadt, and Z. Ram, "Novel, compact, intraoperative magnetic resonance imaging-guided system for conventional neurosorgical operating rooms," *Neurosurgery*, vol. 48, pp. 799–809, 2001.
[9] W. A. Hall, H. Liu, A. J. Martin, C. H. Pozza, R. E. Maxwell, and C. L. Truwit, "Safety, efficacy, and functionality of high-field strength interventional magnetic resonance imaging for neurosurgery," *Neurosurgery*, vol. 46, pp. 632–642, 2000.
[10] C. Nimsky, O. Ganslandt, P. Hastreiter, and R. Fahlbush, "Intraoperative compensation for brain shift," *Surgical Neurol.*, vol. 56, pp. 357–65, 2001.
[11] G. J. Rubino, K. Farahani, D. McGill, B. Van de Wiele, J. P. Villablanca, and A. Wang-Mathieson, "Magnetic resonance imaging-guided neurosurgery in the magnetic fringe fields: The next step in neuronavigation," *Neurosurgery*, vol. 46, pp. 643–654, 2000.

[12] C. R. Wirtz, M. M. Bonsanto, M. Knauth, V. M. Tronnier, F. K. Albert, A. Staubert, and S. Kunze, "Intraoperative magnetic resonance imaging to update interactive navigation in neurosurgery: Method and preliminary experience," *Comput. Aided Surg.*, vol. 2, pp. 172–179, 1997.

[13] G. Unsgaard, A. Gronningsaeter, S. Ommedal, and T. A. N. Hernes, "Brain operations guided by real-time two-dimensional ultrasound: New possibilities as a result of improved image quality," *Neurosurgery*, vol. 51, no. 2, pp. 402–412, 2002.

[14] M. M. Bonsanto, A. Staubert, C. R. Wirtz, V. Tronnier, and S. Kunze, "Initial experience with an ultrasound-integrated single-rack neuronavigation system," *Acta Neurochirurgica*, vol. 143, no. 11, pp. 1127–1132, 2001.

[15] R. D. Bucholz, K. R. Smith, K. A. Laycock, and L. L. McDurmont, "Three-dimensional localization: From image-guided surgery to information-guided therapy," *Methods (Duluth)*, vol. 25, no. 2, pp. 186–200, 2001.

[16] R. M. Comeau, A. F. Sadikot, A. Fenster, and T. M. Peters, "Intraoperative ultrasound for guidance and tissue shift correction in image-guided neurosurgery," *Med. Phys.*, vol. 27, pp. 787–800, 2000.

[17] H. Erbe, A. Kriete, A. Jödicke, W. Deinsberger, and D. K. Böker, "3D-ultrasonography and imaging matching for detection of brain shift during intracranial surgery," in *Computer Assisted Radiology: Proc. Int. Symp. Computer and Communication Systems for Image Guided Diagnosis and Therapy*, 1996, pp. 225–230.

[18] A. Gronningsaeter, A. Kleven, S. Ommedal, T. E. Aarseth, T. Lie, F. Lindseth, T. Lango, and G. Unsgard, "Sonowand, an ultrasound-based neuronavigation system," *Neurosurgery*, vol. 47, no. 6, pp. 1373–1379, Dec. 2000.

[19] A. Jödicke, W. Deinsberger, H. Erbe, A. Kriete, and D.-K. Böker, "Intraoperative three-dimensional ultrasonography: An approach to register brain shift using multidimensional image processing," *Minimally Invasive Neurosurg.*, vol. 41, pp. 13–19, 1998.

[20] N. Pagoulatos, W. S. Edwards, D. R. Haynor, and Y. Kim, "Interactive 3-D registration of ultrasound and magnetic resonance images based on magnetic position sensor," *IEEE Trans. Inform. Technol. Biomed.*, vol. 3, pp. 278–288, Dec. 1999.

[21] J. W. Trobaugh, W. D. Richard, K. R. Smith, and R. D. Bucholz, "Frameless sterotactic ultrasonography: Method and applications," *Computerized Med. Imag. Graphics*, vol. 18, no. 4, pp. 235–246, 1994.

[22] C. D. Barry, C. P. Allott, and N. W. John, "Three-dimensional freehand ultrasound: Image reconstruction and volume analysis," *Ultrasound Med. Biol.*, vol. 23, pp. 1209–1224, 1997.

[23] J. M. Blackall, D. Ruechert Jr, C. R. Maurer, G. P. Penney, D. L. G. Hill, and D. J. Hawkes, "An image registration approach to automated calibration for freehand 3D ultrasound," *Med. Image Computing Comput.-Assist. Intervention*, pp. 462–471, 2000.

[24] F. Lindseth, T. Lango, J. Bang, and T. A. N. Hernes, "Accuracy evaluation of 3D ultrasound-based neuronavigation system," *Comput. Aided Surg.*, vol. 7, pp. 197–222, 2002.

[25] X. Pennec, P. Cachier, and N. Ayache, "Tracking brain deformations in time sequences of 3D US images," *Pattern Recogn. Lett.*, vol. 24, pp. 801–813, 2003.

[26] M. I. Miga, K. D. Paulsen, P. J. Hoopes, F. E. Kennedy, A. Hartov, and D. W. Roberts, "*In vivo* modeling of interstitial pressure in the brain under surgical load using finite elements," *J. Biomech. Eng.*, vol. 122, pp. 354–365, Aug. 2000.

[27] K. E. Lunn, "Co-registration of ultrasound and MR as sparse data for brain deformation model," masters thesis, Thayer School of Engineering, Hanover, NH, 2001.

[28] (2000) Polaris. Northern Digital Inc., Waterloo, ON, Canada. [Online]. Available: http://www.ndigital.com/polaris.html

[29] K. A. Ganser, H. Dickhaus, A. Staubert, M. M. Bonsanto, C. R. Wirtz, V. M. Tronnier, and S. Kunze, "Quantification of brain shift effects in MRI images," *Biomed. Tech. (Berl)*, vol. 42, pp. 247–8, 1997.

[30] A. Nabavi, P. M. Black, D. T. Gering, C. F. Westin, V. Mehta, R. S. Pergolizzi, M. Ferrant, S. K. Warfield, N. Nata, R. B. Schwartz III, W. M. Wells, R. Kikinis, and F. A. Jolesz, "Serial intraoperative magnetic resonance imaging of brain shift," *Neurosurgery*, vol. 48, no. 4, pp. 787–798, Apr. 2001.

[31] C. Nimsky, O. Ganslandt, S. Cerny, P. Hastreiter, G. Greiner, and R. Falbusch, "Quantification of, visualization of, and compensation for brain shift using intraoperative magnetic resonance imaging," *Neurosurgery*, vol. 47, p. 5, 2000.